Chapter 6

[SO_3H/SO_3] Functionalized 2D-MoS2 Nanosheets for Photocatalysis of Organic Pollutants

6.1 Introduction

The chapter presents the effect of SO_3H/SO_3 functionalized 2D-MoS_2 synthesis and their structural characterizations followed by application in photocatalysis. Layered 2D semiconductors like transition metal di-chalcogenides (TMDs) have become a research hotspot due to their unconventional physiochemical, electronic, and optical properties.[1-6] Among these 2D layered materials, molybdenum sulfide (MoS_2) has garnered immense interest due to its variety of use in sodium and lithium-ion batteries[7, 8], photocatalysis[9, 10], lubrication[11], optoelectronics[12], supercapacitors[13], transistors[14], hydrogen evolution reaction (HER)[15, 16], sensors[17], and biomedical applications[18]. In particular, 2D MoS_2 exhibits tunable bandgap (1.2 eV to 1.8 eV, visible to near-infrared), high chemical reactivity, low toxicity, more catalytically active sites, a large surface-to-volume ratio, and high charge-carrier mobility with broad absorption in the visible light range, which makes it an excellent catalyst for visible-light-driven redox reactions [19-23]. The crystalline MoS_2 consists of basal and edge planes, where the former is inherently and thermodynamically favored to have higher surface exposure [24]. Despite this, the photocatalytic activity of MoS_2 is often limited as a result of its dependency on the availability of edge sites [10]. Therefore, many studies have been devoted to improving the exposure of MoS_2 edge sites through nano-engineering (size, morphology, number of layers, defect) [25-27], composition tuning (doping with foreign transition metals, P, N, O, and alloying) [15, 28, 29], phase conversion (2H to 1T) [30], expansion of the interlayer distance [31], and molecular functionalization [32].

On the other hand, the interlayer engineering of MoS_2 nanosheets could have extraordinary potential in improving catalytic activity, and the area is yet to be exploited. Specifically, expansion of the interlayer spacing of 2D-MoS_2 not only significantly improves diffusion kinetics of ions but also increases catalytically active-sites for the charge transfer, enhances

the surface area, fine-tunes electronic structure, and reduces diffusion barriers [33, 34]. For example, Gao et al. synthesized interlayer expanded MoS_2 (9.4 Å) by microwave-assisted method with tailored electronic structure and electrical conductivity. They showed that MoS_2 interlayer expansion incorporates higher number of catalytically active edge-sites, which can lead to improving the performance of MoS_2 for hydrogen evolution reaction (HER) [35]. Similarly, Zhou et al. reported the solvothermal synthesis of oxygen incorporated MoS_2 nanosheets with expanded interlayers (8.4 Å), which was favorable for intercalating foreign ions (OH^-), thereby, improved pseudo-capacitive performance [36]. Also, Lai et al. showed interlayer expanded MoS_2 where and the layer-expanded MoS_2 exhibited high photocatalytic activity [21]. However, the chemical functionalization of MoS_2 nanosheets are still limited and can be accomplished by various means of modifying non-covalent or covalent bonding interaction with metal, non-metal as well as with other organic molecules [37]. In specific, it is always worthwhile to functionalize 2D-MoS_2 for enhancing catalytic activity while creating an expanded interlayer-structure and increased bandgap for improving its functionalities from catalysis to photocatalysis.

Acids are an important class of chemical species characterized by the unique ability to either donate H^+ ions or form a covalent bonding with an electron pair [38]. Sulfonic acid (-SO_3H) groups are especially attractive catalysts due to their metal free composition, low cost, high environmental stability, strong acidity, and non-oxidizing [39]. Functionalization of MoS_2 layers with the large molecules like -SO_3H could have a promising choice to increase the interlayer spacing of 2D-MoS_2 and modify the electronic structure of 2D-MoS_2 and enhance the photocatalytic activity. Bitaraf et al. reported that chemically grafting of -SO_3H functional group on the surface of photocatalyst materials can provide the required H^+ during the reaction and improved the photocatalytic activity [40]. Hyun Gu Kang et al. reported that the methylene blue (MB) dye degradation by using the -SO_3H/-SO_3^- functional group due to the

electrostatic attraction and the cation exchange process between the organic building block of $-SO_3H/-SO_3^-$ functional group and methylene blue molecules [41].

In this work, we demonstrate the synthesis of sulfonic acid/sulfur trioxide (SO_3H/SO_3) functionalized MoS_2 nanosheets by a one-pot hydrothermal method. The structure and morphology were investigated by Raman, X-ray diffraction (XRD), scanning electron microscopy (SEM), transmission electron microscopy (TEM), while chemical composition, bonding, and degree of functionalization was confirmed by using X-ray photoelectron spectroscopy (XPS) and Fourier transform infrared spectroscopy (FTIR). Furthermore, we demonstrate the photocatalytic activity of SO_3H/SO_3-MoS_2 in Methylene Blue (MB) aqueous solution as a function of time and dye concentration. Also, we determine the catalytic activity of the SO_3H/SO_3-MoS_2 by calculating the rate kinetics of the dye degradation followed by establishing the mechanism of the light-driven redox process. Finally, we compared the efficacy of the 2D SO_3H/SO_3-MoS_2 nanosheets with other pristine 2D-MoS_2 nanosheets and commercially available bulk MoS_2 along with their kinetics of the redox process under an identical environment.

6.2 Results and discussions

The sulfonic acid/sulfur trioxide (SO_3H/SO_3) group functionalized 2D-MoS_2 was synthesized using a one-pot hydrothermal synthesis method as discussed in detail in the section 2.1.9 of chapter 2. The as-obtained functionalized 2D-MoS_2 nanosheet was characterized using various spectroscopic and microscopic techniques (e.g., FTIR, UV-Vis, Raman spectroscopy, TEM/HRTEM, SEM, etc.) as discussed in-detail in chapter 2 (section 2.2).

The Fourier transform infrared (FTIR) measurement was carried out to obtain the bending and stretching vibration of the SO_3H/SO_3 functional group present in MoS_2 nanosheets as shown in Figure 6.1a. Absorption bands observed at 460 cm^{-1} and 593 cm^{-1} are refers to the Mo-S stretching vibration [42]. Absorption band at 1056 cm^{-1} corresponds to S=O (SO_3^-)

stretching modes of the SO_3H [43, 44]. Another two absorption bands at 1227 cm^{-1} and 1405 cm^{-1} are associated with the O=S=O stretching mode of the SO_3H [44, 45]; while the two absorption bands at 1159 cm^{-1} and 1198 cm^{-1} are indicating the presence of SO_3 molecule [40]. A band at 1626 cm^{-1} (O-H) are corresponding to the surface absorbed water molecule. The FTIR spectrum indicates that the as-prepared MoS_2 sample exhibits the Mo-S bands, and the formation of the SO_3H/SO_3 group (S=O and O=S=O) signifies the functionalization of the SO_3H/SO_3 functional group on the surface of MoS_2 nanosheets. Raman spectrum in Figure 6.1b shows successive peaks at 376.75, 404.67, 452, 585.5, 744.10, and 814 cm^{-1} assigned to the E^1_{2g}, A_{1g}, 2LA, E_{1g}, $2E_{2g}$, and A_{1g} band of 2D MoS_2 ,respectively; while the and 1013 cm^{-1} corresponds to the SO_3H/SO_3 vibration mode [46, 47]. The vibration at ~1013 cm^{-1} in MoS_2 demonstrates the signature of the SO_3H group, which is covalently bonded with the 2D-MoS_2 [48]. Figure 6.1c shows the XPS spectrum of S 2p, which represents the S $2p_{3/2}$ and S $2p_{1/2}$ spin-orbit doublets at their respective positions of 162.08 eV and 163.26 eV [15, 49]. Figure 6.1c also shows a broad and low-intensity XPS peak at higher binding energy and after deconvolution, two successive peaks of S $2p_{3/2}$ and S $2p_{1/2}$ were obtained at 168.8 eV and 169.8 eV, respectively. Such S $2p_{3/2}$ and S $2p_{1/2}$ peaks at high binding energies suggest the formation of S-OH and S=O bonding, which are a typical signature of SO_3H chemical group covalently attached to the MoS_2 nanosheets, while another peak at higher binding energy at 166.6 eV are corresponding to the SO_3 group as discussed in FTIR section [40, 50]. On the other hand, O 1s spectrum shown in Figure 6.1d depicts two oxygen peaks at 532.01 eV and 533.18 eV implying the existence of S-OH and S=O bonds, respectively. In this regard, such S-HO and S=O bonds again validate the SO_3H/SO_3 groups covalently attached to the MoS_2 nanosheets [51]. This further justifies the successful formation of sulfonic acid/sulfur trioxide functionalized 2D-MoS_2 during the one-pot hydrothermal process.

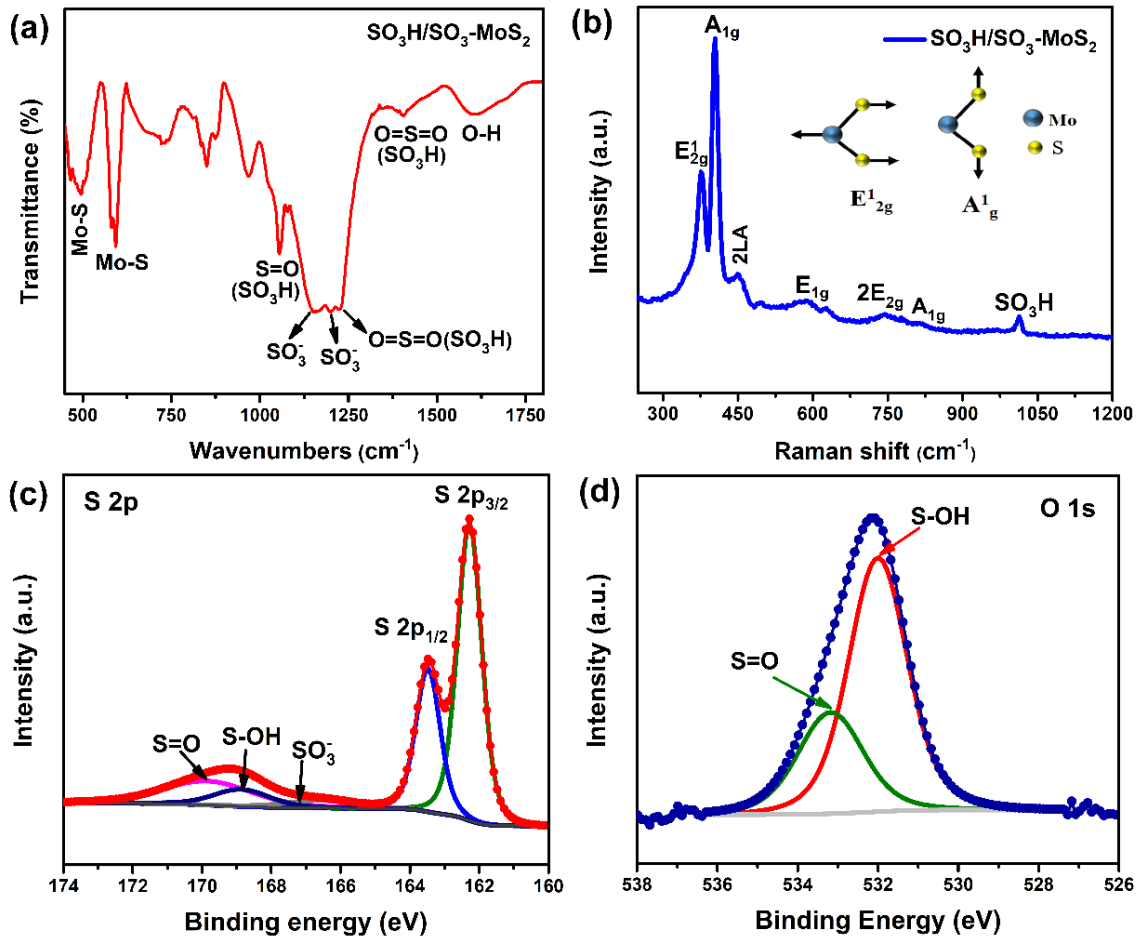

***Figure 6.1**: Shows (a) Fourier transform infrared (FTIR) spectrum of SO_3H/SO_3-MoS_2; (b) Raman spectra of the SO_3H/SO_3 -MoS_2 nanosheets; (c) & (d) high-resolution S 2p XPS spectrum and O1s XPS spectrum, respectively.*

The crystal structure and phase analysis of as-synthesized SO_3H/SO_3-MoS_2 nanosheets were analyzed using the low-angle X-ray diffraction (XRD) method as shown in Figure 6.2. The SO_3H/SO_3-MoS_2 nanosheets exhibit distinct diffraction peaks (blue colure Figure 6.2) at 9.46°, 17.90°, 32.88°, 57.47°, which confirms characteristics 2D-MoS_2 planes of (002), (004), (010), and (110), respectively. It was found that the (002) peak of pristine 2D-MoS_2 is shifted towards lower angle in SO_3H/SO_3-MoS_2 as shown in Figure 6.2. The corresponding d-spacing of the (002) plane was found to be 9.4 Å as calculated via Bragg's equation. The difference between the d-spacing indicated the formation of a new lamellar structure with the

enlarged interlayer spacing of 9.4 Å compared with 6.3 Å in pristine 2D-MoS_2 (P-MoS_2) (green colure Figure 6.2) [31]. A new peak emerges at 17.90° in SO_3H/SO_3-MoS_2 (blue curve) corresponds to the characteristics plane of (004) of 2D-MoS_2, which could be due to the successive expansion of interlayers [31]. It is assumed that the (002) d-spacing enlargement is primarily due to the adsorption and intercalation of the SO_3H/SO_3 functional group between successive MoS_2 layers as demonstrated in the TEM part in the next section. Besides, two higher angle peaks of 32.78° of (010) and 57.44° of (110) (blue colure Figure 6.2) indicates that the MoS_2 crystal structure remains intact (specifically, the basal planes) even after the SO_3H/SO_3 functionalization.

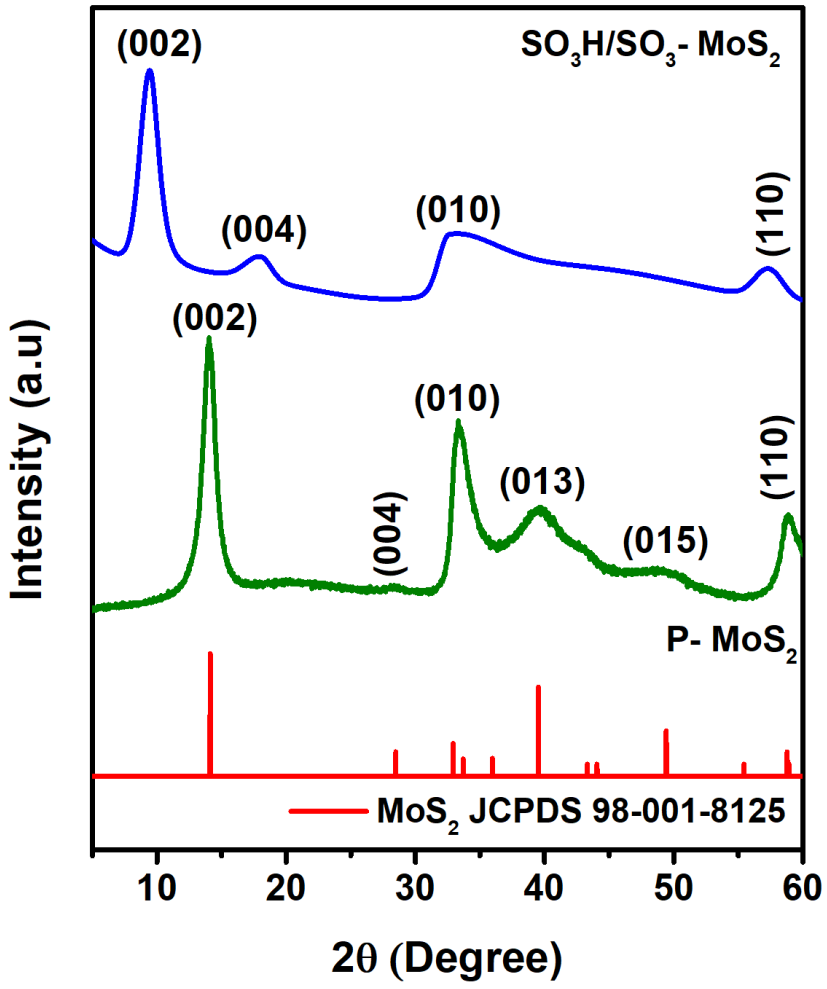

Figure 6.2: *XRD diffraction pattern of as-synthesized MoS_2 (Pristine MoS_2) with the interlayer spacing (d) of 6.3 Å and SO_3H/SO_3-MoS_2 with the interlayer spacing (d) of 9.4 Å.*

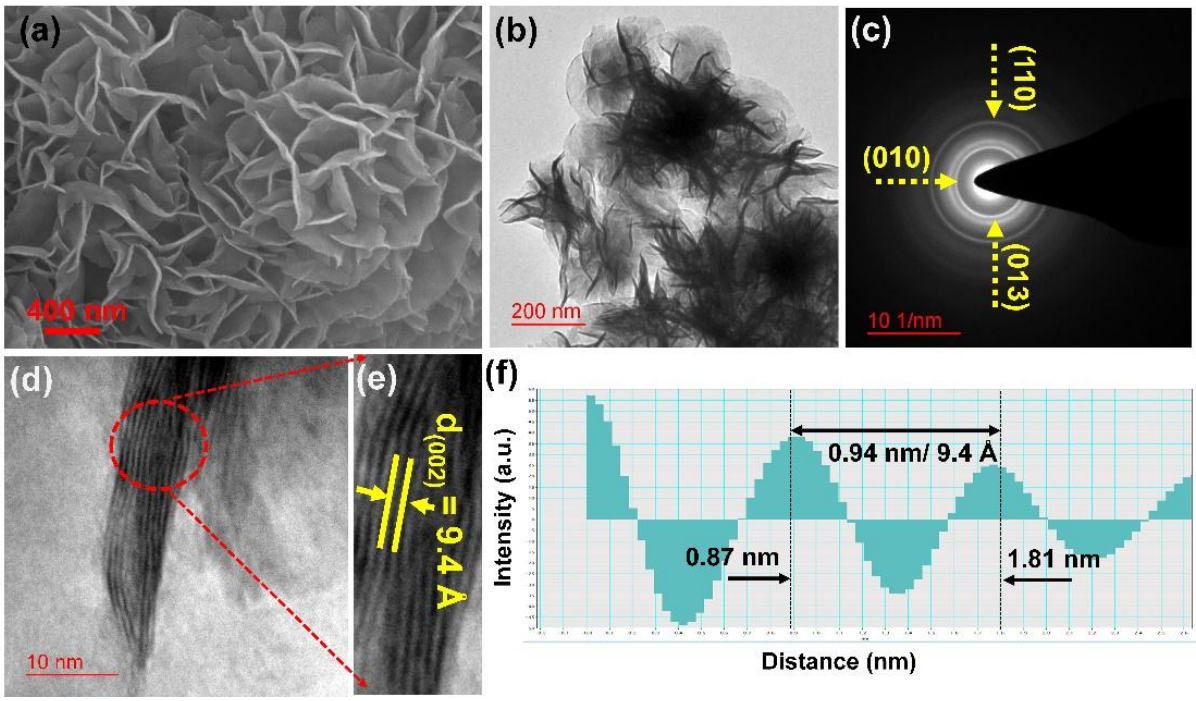

Figure 6.3: *Shows (a) SEM images demonstrating morphology of SO_3H/SO_3 functionalized MoS_2 nanosheets; (b) the bright-field transmission electron micrograph of as-synthesized SO_3H/SO_3-MoS_2; (c) electron diffraction pattern; (d) & (e) illustrate HRTEM depicting the interlayer d-spacing of functionalized 2D-MoS_2; (f) line intensity profile of the line drawn in the inverse FFT image.*

Scanning electron microscopy (SEM) and transmission electron microscopy (TEM) were performed to investigate the morphology and structure of as-synthesized SO_3H/SO_3-MoS_2. Figure 6.3a shows the nanoflower-like morphology of as-synthesized 2D SO_3H/SO_3-MoS_2 with a flaky petal-like morphology of 2D nanosheets. The sharp edge of SO_3H/SO_3-MoS_2 nanosheets exhibits more active electron transfer sites, which we believe take part in a faster light-driven redox process, thus, imparting the high-performance catalytic activity. Figure 6.3b shows the transmission electron micrograph of SO_3H/SO_3-MoS_2 nanosheets illustrating the flaky 2D layered morphologies with entangled structure. The TEM image (Figure 6.3b) also demonstrates the ultrathin nanosheets of SO_3H/SO_3-MoS_2 contain ripples and

corrugations in its structure. Figure 6.3c shows the SAED pattern with the characteristic diffraction planes of (010), (013), and (011), suggesting the simple MoS_2 lattice as elucidated in XRD data. The high-resolution TEM (HRTEM) image shown in Figure 6.3 d-f demonstrates the layered crystalline structure of a few-layers of 2D-MoS_2 nanosheet with an increased interlayer spacing of 9.4 Å, which are 3.1 Å larger than the pristine counterpart of 2D-MoS_2 as interpreted in Figure 6.4 from Figure 6.4b SAED data endorse that there were no significant changes occurred in the 2D-MoS_2 basal plane after bonding of SO_3H/SO_3 molecules to the MoS_2 basal plane. The enlarged interlayer spacing of the (002) plane of MoS_2 nanosheets is because of the intercalation of the SO_3H/SO_3 functional group through the MoS_2 inter-layers during the synthesis process.

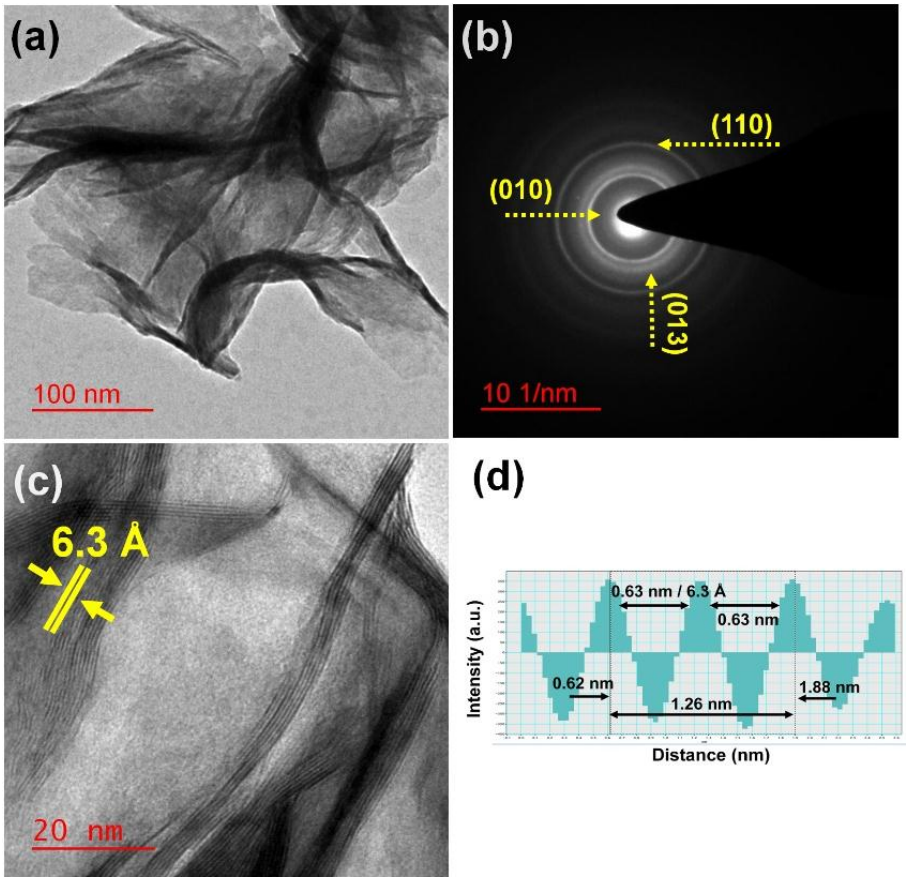

Figure 6.4: *Shows (a) Transmission electron micrograph of pristine 2D-MoS_2 (i.e., P-MoS_2); (b) SAED pattern of pristine 2D-MoS_2 depicts characteristics crystal planes of (110), (013), and (010); (c) the HRTEM images of typical few-layered 2D-MoS_2 with an interplanar*

distance of 6.3 Å; (d) line intensity profile of the line drawn in the inverse FFT image (GATAN Inc., USA).

The photocatalytic activity of SO_3H/SO_3-MoS_2 was investigated in organic methylene blue (MB) dye solution (10 ppm) under visible light irradiation and all the experiments were conducted with different solutions of methylene blue (MB) dye concentrations and various MoS_2 samples (*e.g., The Bulk MoS_2, Pristine 2D-MoS_2, and SO_3H/SO_3-MoS_2*). About 5 mg of various catalysts were added to aqueous solutions of MB dye (e.g., *5 ml of 5 ppm, 5 ml of 10 ppm, and 5 ml of 15 ppm*). The entire assemblies were kept inside of a laboratory-based closed light-chamber with visible white LED source (light intensity: 2 W/m^2, and light spectrum: 360 to 700 nm). Before irradiation, the mixture was stirred under dark condition for a few minutes to attain adsorption-desorption equilibrium and then put them inside of the visible-light chamber. The known amount of solutions have been collected as a function of time, centrifuged, and separated out from the catalysts. Further, the absorption spectra of as-separated solutions were measured in UV-Vis spectrophotometer (JASCO V-770, Japan).

The as-obtained UV-Vis absorption spectra of dye solutions (collected as a function of time) are shown in Figure 6.5. From UV-Vis spectral data of MB solutions after photocatalytic treatment by SO_3H/SO_3-MoS_2, the peak intensity decreases with increasing exposure time and is extremely low (near zero) after 50 minutes of time exposure (for 10 ppm solution), as shown in Figure 6.5a. Figure 6.5b shows the pictographic images of the series of MB dye solutions obtained as a function of time after the photocatalytic reactions with SO_3H/SO_3-MoS_2. It could be seen that with increasing the time of reaction, the blue color of the MB solution became colorless (Figure 6.5b). Also, the photocatalytic activities of SO_3H/SO_3-MoS_2 were performed by varying dye concentrations (e.g., 5 ppm and 15 ppm of MB dye solution) while keeping the amount of catalyst and solution volume constant. It was found

that the catalytic activity proportionally changes with varying dye concentrations, as shown in Figures 6.5c and Figures 6.5 d. Figure 6.5c depicts that the 5 ppm dye solution degraded within 10 min, while the 15 ppm dye took 80 min (Figure 6.5d**)** to degrade after reacting with SO_3H/SO_3-MoS_2 samples under the equilibrium conditions.

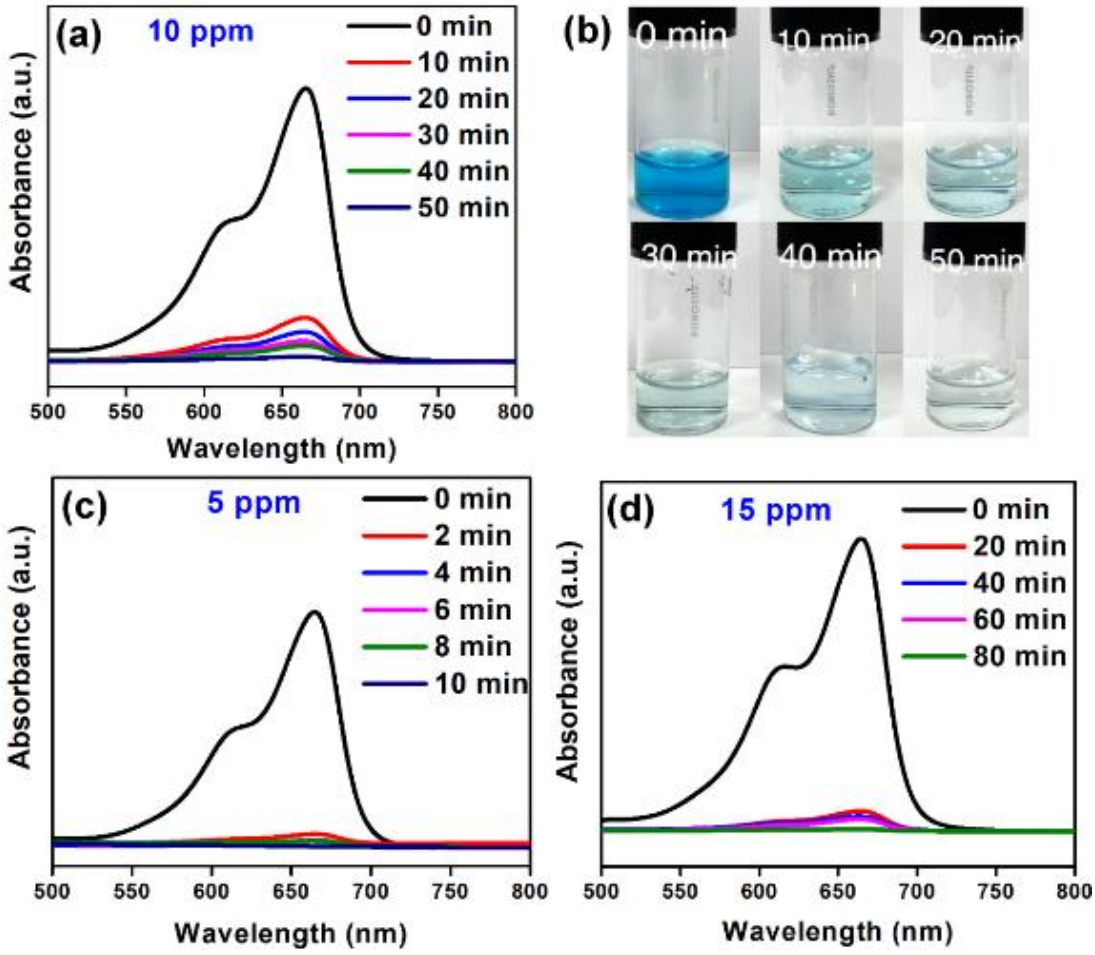

Figure. 6.5*: Shows (a) UV-Vis absorbance spectra of SO_3H/SO_3-MoS_2 as a function of time in 10 ppm MB dye solution; (b) the representative photographic images were taken for studying the comparative photocatalytic activity of SO_3H/SO_3-MoS_2 as a function of time for 10 ppm solution; (c) and (d) illustrates UV-Vis absorbance spectra of SO_3H/SO_3-MoS_2 at 5 ppm & 15 ppm MB dye solutions.*

A similar experiment was carried out to establish the efficacy of SO_3H/SO_3-MoS_2 in comparison with pristine 2D-MoS_2 (P-MoS_2) and commercially available bulk MoS_2 (B-MoS_2) (Sigma-Aldrich, India). Figure 6.6 show the UV-Vis data indicating the photocatalytic activities of B-MoS_2 and P-MoS_2 as a function of time. It was obtained that while reacting with the B-MoS_2 and P-MoS_2, the 10 ppm dye solutions were not completely degraded even after 240 min (i.e., 4 h) (Figure 6.6). The peak intensity of both B-MoS_2 and P-MoS_2 decreases slowly with increasing light exposure time, however, the characteristic peak intensities manifest that the bulk and pristine samples were degraded the MB dye even after 240 min photocatalytic reaction time. Thus, it can be considered that the SO_3H/SO_3-MoS_2 shows better light-driven catalytic activity than B-MoS_2 and P-MoS_2.

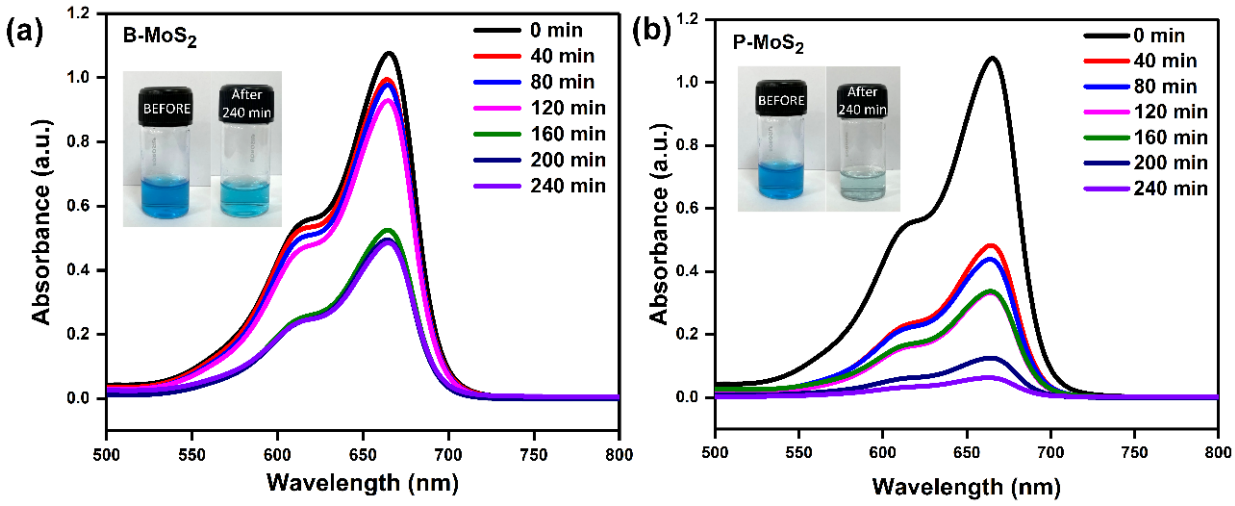

Figure 6.6: *UV-Vis absorbance spectra as a function of time of (a) B-MoS_2; and (b) P-MoS_2 in 10 ppm MB dye.*

To determine the rate kinetics of the photocatalytic reactions, we have plotted the normalized intensity plots from the UV-Vis data as a function of time and calculated the rate kinetics. Figure 6.7a shows normalized intensity (I/I_0) vs. time data where the slope of the curve illustrates the comparative rate of dye degradation as a function of time for different concentrations (ppm-level) of dye, e.g., 5 ppm, 10 ppm, and 15 ppm [52]. The slope of the normalized curves (I/I_0) (Figure 6.7a) suggests that the redox process of dye degradation

decreases with increasing dye concentrations. It is widely reported that initial concentrations of dye pollutants limit the active catalytic sites at the photocatalyst surface. For instance, lower dye concentration occupies fewer active sites leading to effective degradation performance. Furthermore, while comparing the SO_3H/SO_3-MoS_2 with other stereotype MoS_2 samples (i.e., pristine 2D-MoS_2, and commercially available bulk MoS_2) it seems that the catalytic performances degraded gradually from functionalized 2D-MoS_2 to pristine 2D-MoS_2 to the bulk MoS_2 as shown in Figure 6.7b.

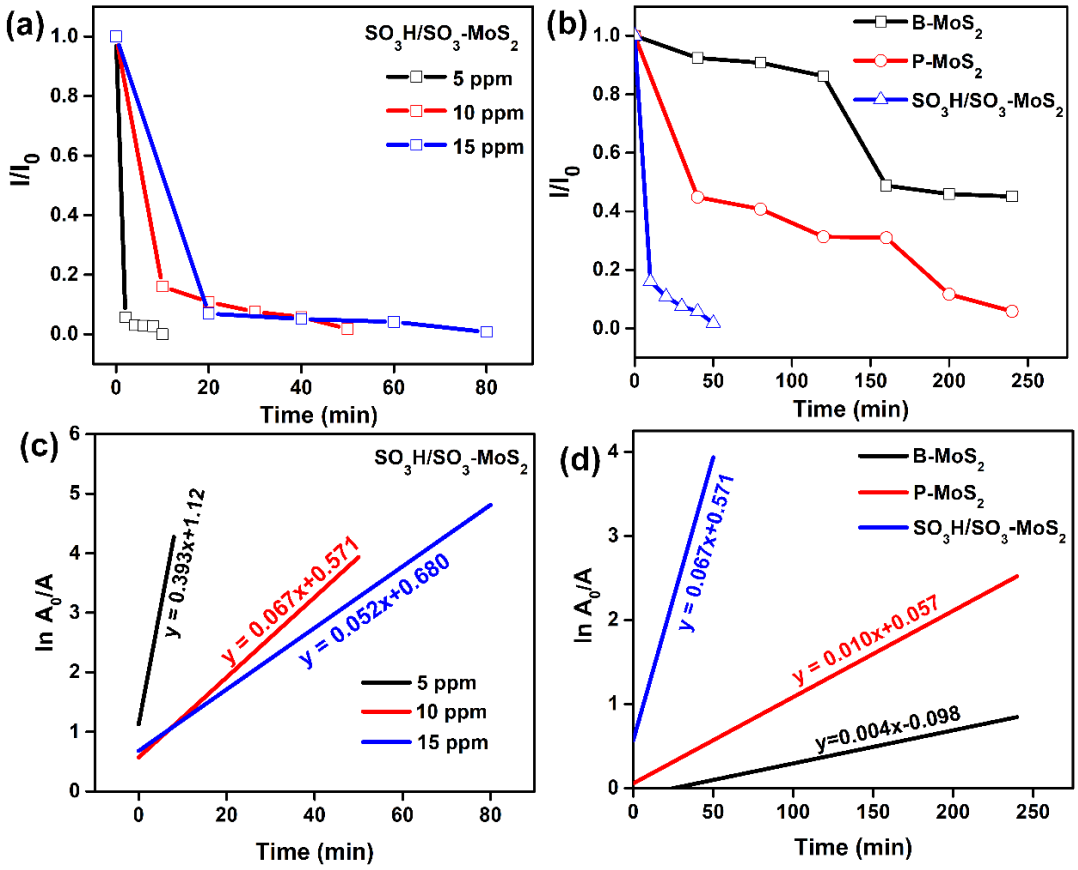

Figure 6.7: *Shows (a) the comparative normalized intensity as a function of time illustrating the rate of MB dye degradation at 5, 10 & 15 ppm solution; (b) comparative normalized intensity plots for SO_3H/SO_3-MoS_2, P-MoS_2, B-MoS_2 and as a function of time illustrating the MB dye degradation rate in 10 ppm dye solution; (c) the comparative rate kinetics plots of photocatalytic dye degradation reactions using the 10 ppm dye solution using SO_3H/SO_3-*

MoS_2; (d) demonstrates the rate kinetics plot of photocatalytic MB degradation using SO_3H/ SO_3-MoS_2, P-MoS_2, and B-MoS_2.

The rate kinetics of MB-dye degradation using various MoS_2 samples is shown in Figure 6.7c and was calculated via Equation 6.1 [52].

$$ln\left(\frac{A_0}{A}\right) = kt \qquad (6.1)$$

Where A_0 and A were the initial and residual absorbance at different time intervals, "*t*" and '*k*' is the first-order rate constant. For SO_3H/SO_3-MoS_2 (Figure 6.7c) the kinetic rate plot shows the highest catalytic activity at 5 ppm dye solution (k =0.39331 min^{-1}). In comparison, lowest for 15 ppm solution (k =0.05165 min^{-1}), and this is obvious that the rate of dye degradation under equilibrium conditions varies as a function of dye concentrations (while the amount of catalyst and volume of the liquid is constant). Similarly, the photocatalytic activity performance was evaluated with various catalysts (i.e., SO_3H/SO_3-MoS_2, P-MoS_2, and B-MoS_2) as shown in Figure 6.7d. The as-calculated k-values for bulk-MoS_2, pristine 2D-MoS_2, and functionalized-MoS_2 are obtained as 0.00394 min^{-1}, 0.01027 min^{-1}, and 0.06728 min^{-1}, respectively, which further manifests the faster electron transfer in SO_3H/SO_3-MoS_2.

In order to understand the better catalytic performance of SO_3H/SO_3 functionalized MoS_2, compared to pristine MoS_2, BET surface area and pore size distribution of both samples were evaluated by nitrogen adsorption isotherm measurements. Both the samples exhibited typical type IV isotherm with H_3 hysteresis loops attributing mesoscale pores in the materials. The BET surface area for sulfonated MoS_2 is 23.5 m^2/g, which is higher compared to the pristine MoS_2 (19.7 m^2/g) as demonstrated in Figure 6.8a. The higher accessible surface area with additional surface functionality makes the SO_3H/SO_3 functionalized MoS_2 catalytically more active for organic dye degradation compared to pristine MoS_2. Further, the enhancement in functionalized 2D-MoS_2 surface area is primarily because of the intercalation of the

SO_3H/SO_3 functional groups through the interlayer as demonstrated earlier of this chapter [i.e., intercalation of functional groups through the (002) layers as discussed in the TEM/HRTEM, and X-ray diffraction section]. To this end, it is obvious that the improvements in the surface area of 2D-MoS_2 play a vital role in catalyzing the faster redox process of MB dye degradation.

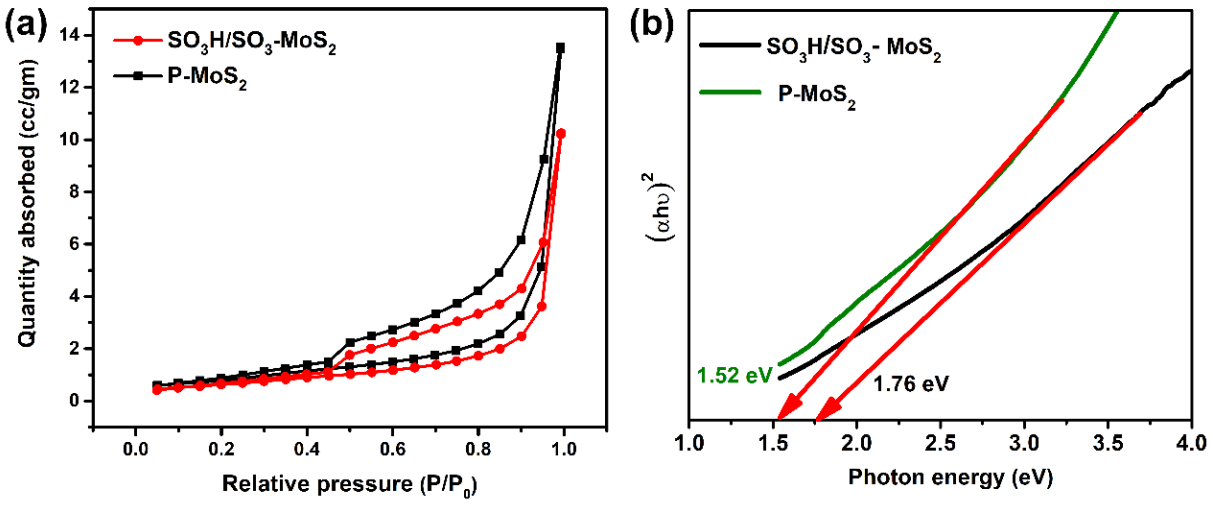

Figure 6.8: *Illustrates (a) the comparative N_2 adsorption/desorption isotherms data of SO_3H/SO_3-MoS_2 and P-MoS_2 obtained during the BET measurement; (b) shows the comparative Tauc plot of P-MoS_2 and SO_3H/SO_3-MoS_2.*

Since the P-MoS_2 exhibited higher catalytic surface area than B-MoS_2, thereby it shows enhanced catalytic performance than B-MoS_2. On the other hand, SO_3H/SO_3-MoS_2 shows much faster photocatalytic activity compared to P-MoS_2 and B-MoS_2 due to its expanded interlayers and functionalized SO_3H/SO_3 molecules covalently attached to 2D-MoS_2, which together accelerate the light-driven electron transfer to the MB-dye for rapid degradation. The bandgap of SO_3H/SO_3-MoS_2 was measured as 1.76 eV compared to the P-MoS_2, which was 1.52 eV as depicted in Figure 6.8b. The widening of MoS_2 bandgap could be due to the covalent functionalization of the 2D-MoS_2 using SO_3H/SO_3 molecule.

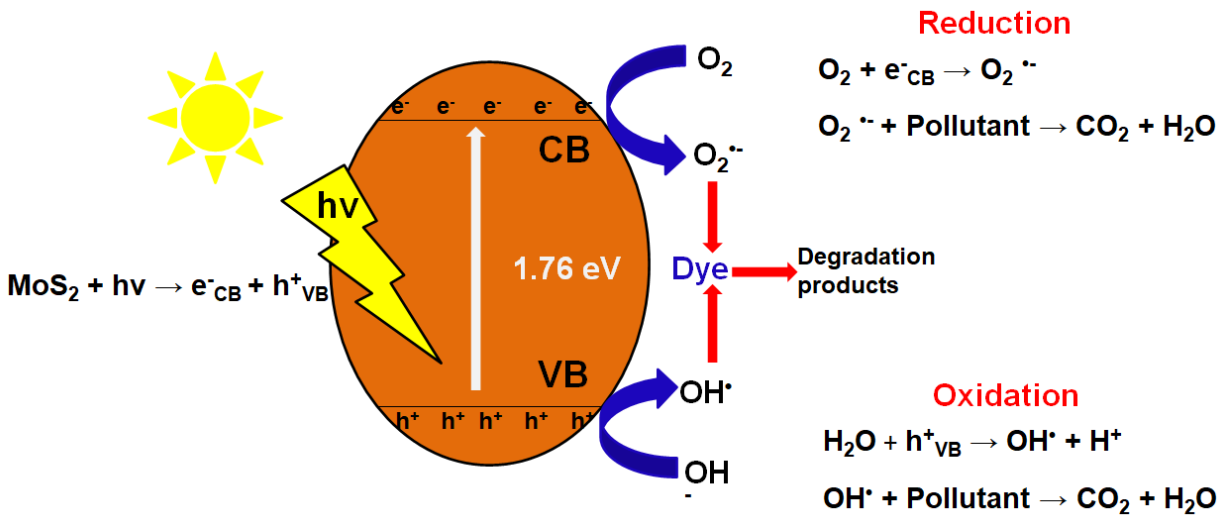

Figure 6.9: *Schematic illustrating the mechanism of dye degradation using functionalized-MoS_2 samples.*

Following the above results, a possible mechanism is interpreted and shown in Equations 6.2 to Equations 6.7 [53-55]. In the first step, when visible light was irradiated on the MoS_2, the photons were absorbed, and the electrons were excited from the valence band (VB) to the conduction band (CB), as explained in Equation 6.2 and illustrated in Figure 6.9. The resultant photoelectron at the CB and the holes at the VB further migrate through the surface of MoS_2, which can participate in the respective reduction and oxidation reactions. Here, the chemisorbed H_2O molecules and OH^- ions interact with conduction band electrons that produce superoxide anion radicals $O_2^{\bullet-}$ as shown in Equation 6.3. In the next step, valence band holes are responsible for forming $OH^{\bullet}$ radicals as given in Equation 6.4 (Figure 6.9).

$$MoS_2 + h\nu \rightarrow e^-_{CB}\ (MoS_2) + h^+_{VB}\ (MoS_2) \qquad (6.2)$$

$$e^-_{CB} + O_2 \rightarrow O_2^{-\cdot} \qquad (6.3)$$

$$h^+_{VB} + OH^- \rightarrow OH^{\cdot} \qquad (6.4)$$

Finally, various forms of active oxygen species such as $O_2^{\bullet-}$, $OH^{\bullet}$, $OH^{\bullet-}$, OH^-, $HO_2^{\bullet}$, and H_2O_2 are produced from the following successive processes, which could be responsible for the degradation of MB dye as demonstrated in Equation 6.5, Equation 6.6, and Equation 6.7.

$$O_2^{-\cdot} + H_2O \rightarrow HO_2^{\cdot} + OH^{\cdot -} \quad (6.5)$$

$$HO_2^{\cdot} + H_2O \rightarrow H_2O_2 + OH^{\cdot} \quad (6.6)$$

$$H_2O_2 + O_2^{-\cdot} \rightarrow H_2O_2 + OH^{\cdot} + O_2 \quad (6.7)$$

The efficiency of MoS_2 photo-degradation is primarily improved by inhibiting photo-induced e^- and h^+ pair recombination and extending absorption to the visible-light region as demonstrated in Figure 4c. The higher band gap of SO_3H/SO_3-MoS_2 favors the separation of electrons and holes, which facilitates SO_3H/SO_3-MoS_2 to be performed as a high-performance photocatalyst. The rate-enhancement in photocatalytic dye degradation kinetics of SO_3H/SO_3-MoS_2 apparently due to the following reasons: (i) the bandgap widening results in the more light absorption followed by the low charge-recombination, (ii) the expanded 2D-MoS_2 interlayers introduce more catalytically active edge-plane like sites; (iii) the improved surface adsorption/desorption of organic compounds owing to the surface SO_3H/SO_3 molecules; and (iv) the enhanced redox properties as a results of the faster charge-transfer. It seems that the higher the SO_3H/SO_3 surface coverage, the more effective charge transfer occurs, resulting in the better oxidation of the catalyst itself [41]. We believe that the SO_3H/SO_3 functionalized 2D-MoS_2 surface can provide the required H^+ during the reaction and improve the photocatalytic activity compared with bulk-MoS_2 and pristine 2D-MoS_2.

6.3 Chapter summary

In summary, we have successfully demonstrated the enhanced catalytic activity of sulfonic acid/sulfur trioxide (SO_3H/SO_3) functionalized 2D-MoS_2 nanosheets to degrade methylene

blue dye. The SO_3H/SO_3-MoS_2 nanosheets were synthesized via hydrothermal method followed by structural and spectroscopic characterizations. Functionalization of 2D-MoS_2 was confirmed by Raman spectroscopy, FTIR, and XPS and found that the SO_3H/SO_3 molecules were covalently attached with the MoS_2 nanosheets. X-ray diffraction associated with SEM, HRTEM, and SAED illustrated that no significant changes occurred in the 2D-MoS_2, except the expansion of (002) interlayers of ~3.1 Å. The photocatalysis experiments show that the SO_3H/SO_3-MoS_2 exhibits enhanced activity of the redox reaction, which is primarily due to the widening of MoS_2 bandgap, enhanced surface area, introduction of a large amount of active catalytic sites, successively increased free electrons, and above all, the functional group attached to the MoS_2 nanosheets. The mechanism of faster rate kinetics in SO_3H/SO_3-MoS_2 was elucidated and found that possibly various active oxygen species formed followed by light-driven charge transfer to the organic dye to degrade it. We believe that the expanded interlayer in SO_3H/SO_3-MoS_2 improves the ion diffusion kinetics in aqueous solution, increases surface area and catalytically active surface sites while reducing the diffusion barriers, thereby faster the light-driven charge transfer for the redox reaction. We believe that SO_3H/SO_3 functionalized 2D-MoS_2 with expanded interlayers could open up enormous possibilities of other 2D materials functionalization for wider applications, such as the removal of toxic pollutants, catalysis of organic molecules, heavy metal ions adsorption or removal, hydrogen evolution, enhanced redox process for electrochemical devices (psuedocapacitors, batteries), biomedical devices, and so on.

Reference

[1] M.-h. Wu, L. Li, N. Liu, D.-j. Wang, Y.-c. Xue, and L. Tang, "Molybdenum disulfide (MoS_2) as a co-catalyst for photocatalytic degradation of organic contaminants: A review," *Process Safety and Environmental Protection*, vol. 118, pp. 40-58, 2018.

[2] M. Chhowalla, H. S. Shin, G. Eda, L.-J. Li, K. P. Loh, and H. Zhang, "The chemistry of two-dimensional layered transition metal dichalcogenide nanosheets," *Nat. Chem.*, vol. 5, no. 4, pp. 263-275, 2013.

[3] N. N. Rosman *et al.*, "Photocatalytic properties of two-dimensional graphene and layered transition-metal dichalcogenides based photocatalyst for photoelectrochemical hydrogen generation: An overview," *International Journal of Hydrogen Energy*, vol. 43, no. 41, pp. 18925-18945,2018.

[4] F. Haque, T. Daeneke, K. Kalantar-zadeh, and J. Z. Ou, "Two-Dimensional Transition Metal Oxide and Chalcogenide-Based Photocatalysts," *Nano-Micro Letters*, vol. 10, no. 2, p. 23, 2017.

[5] S. Das, M. Kim, J.-w. Lee, and W. Choi, "Synthesis, Properties, and Applications of 2-D Materials: A Comprehensive Review," *Crit. Rev. Solid State Mater. Sci.*, vol. 39, no. 4, pp. 231-252, 2014.

[6] B. Fang, Z. Xing, D. Sun, Z. Li, and W. Zhou, "Hollow semiconductor photocatalysts for solar energy conversion," *Advanced Powder Materials*, vol. 1, no. 2, p. 100021, 2022.

[7] J. Wu *et al.*, "Dual-phase MoS_2 as a high-performance sodium-ion battery anode," *J. Mater. Chem. A*, 10.1039/C9TA11913B vol. 8, no. 4, pp. 2114-2122, 2020.

[8] T. Stephenson, Z. Li, B. Olsen, and D. Mitlin, "Lithium ion battery applications of molybdenum disulfide (MoS_2) nanocomposites," *Energy Environ. Sci.*, vol. 7, no. 1, pp. 209-231, 2014.

[9] G. Chandrabose *et al.*, "Removal and degradation of mixed dye pollutants by integrated adsorption-photocatalysis technique using 2D MoS_2/TiO_2 nanocomposite," *Chemosphere*, vol. 279, p. 130467, 2021/09/01/ 2021.

[10] H. K. Sadhanala, S. Senapati, K. V. Harika, K. K. Nanda, and A. Gedanken, "Green synthesis of MoS_2 nanoflowers for efficient degradation of methylene blue and crystal violet dyes under natural sun light conditions," *New J. Chem.,* 10.1039/C8NJ01731J vol. 42, no. 17, pp. 14318-14324, 2018, doi: 10.1039/C8NJ01731J.

[11] W. O. Winer, "Molybdenum disulfide as a lubricant: A review of the fundamental knowledge," *Wear,* vol. 10, no. 6, pp. 422-452, 1967/11/01/ 1967.

[12] H. Wang, C. Li, P. Fang, Z. Zhang, and J. Z. Zhang, "Synthesis, properties, and optoelectronic applications of two-dimensional MoS_2 and MoS_2-based heterostructures," *Chem. Soc. Rev.,* 10.1039/C8CS00314A vol. 47, no. 16, pp. 6101-6127, 2018, doi: 10.1039/C8CS00314A.

[13] D. Sarkar *et al.,* "Expanding Interlayer Spacing in MoS_2 for Realizing an Advanced Supercapacitor," *ACS Energy Lett.,* vol. 4, no. 7, pp. 1602-1609, 2019/07/12 2019.

[14] H. Kwon *et al.,* "Monolayer MoS_2 field-effect transistors patterned by photolithography for active matrix pixels in organic light-emitting diodes," *npj 2D Materials and Applications,* vol. 3, no. 1, p. 9, 2019/02/19 2019, doi: 10.1038/s41699-019-0091-9.

[15] V. K. Singh, U. Gupta, B. Mukherjee, S. Chattopadhyay, and S. Das, "MoS_2 Nanosheets on $MoNi_4/MoO_2$ Nanorods for Hydrogen Evolution," *ACS Appl. Nano Mater.,* vol. 4, no. 1, pp. 886-896, 2021/01/22 2021, doi: 10.1021/acsanm.0c03296.

[16] U. Sharma, S. Karazhanov, R. Jose, and S. Das, "Plasmonic hot-electron assisted phase transformation in 2D-MoS_2 for the hydrogen evolution reaction: current status and future prospects," *Journal of Materials Chemistry A,* 10.1039/D1TA10918A vol. 10, no. 16, pp. 8626-8655, 2022, doi: 10.1039/D1TA10918A.

[17] W. Zhang, P. Zhang, Z. Su, and G. Wei, "Synthesis and sensor applications of MoS_2-based nanocomposites," *Nanoscale,* 10.1039/C5NR06121K vol. 7, no. 44, pp. 18364-18378, 2015, doi: 10.1039/C5NR06121K.

[18] T. Liu and Z. Liu, "2D MoS_2 Nanostructures for Biomedical Applications," *Adv. Healthcare Mater.,* vol. 7, no. 8, p. 1701158, 2018.

[19] Q. H. Wang, K. Kalantar-Zadeh, A. Kis, J. N. Coleman, and M. S. Strano, "Electronics and optoelectronics of two-dimensional transition metal dichalcogenides," *Nat. Nanotechnol,* vol. 7, no. 11, pp. 699-712, 2012.

[20] S. V. P. Vattikuti, P. C. Nagajyothi, and J. Shim, "Use of lactic acid modified MoS_2 nanopetals to improve photocatalytic degradation of organic pollutants," *Mater. Res. Express,* vol. 5, no. 9, p. 095016, 2018.

[21] M. T. L. Lai *et al.,* "The improved photocatalytic activity of highly expanded MoS_2 under visible light emitting diodes," *Nanoscale Adv.,* 10.1039/D0NA00936A vol. 3, no. 4, pp. 1106-1120, 2021, doi: 10.1039/D0NA00936A.

[22] A. Rani *et al.,* "Visible light driven photocatalysis of organic dyes using SnO_2 decorated MoS_2 nanocomposites," *Chemical Physics Letters,* vol. 738, p. 136874, 2020.

[23] A. Devadoss, N. Srinivasan, V. P. Devarajan, A. N. Grace, and S. Pitchaimuthu, "8 - Electrocatalytic properties of two-dimensional transition metal dichalcogenides and their hetrostructures in energy applications," in *2D Nanoscale Heterostructured Materials,* S. Jit and S. Das Eds.: Elsevier, 2020, pp. 215-241.

[24] D. Y. Chung *et al.,* "Edge-exposed MoS_2 nano-assembled structures as efficient electrocatalysts for hydrogen evolution reaction," *Nanoscale,* vol. 6, no. 4, pp. 2131-2136, 2014, doi: 10.1039/C3NR05228A.

[25] J. Xie *et al.*, "Defect-Rich MoS_2 Ultrathin Nanosheets with Additional Active Edge Sites for Enhanced Electrocatalytic Hydrogen Evolution," *Adv. Mater.,* vol. 25, no. 40, pp. 5807-5813, 2013.

[26] W. Qiao *et al.*, "Monolayer MoS_2 quantum dots as catalysts for efficient hydrogen evolution," *RSC Adv.,* vol. 5, no. 118, pp. 97696-97701, 2015.

[27] S. Li *et al.*, "Edge-Enriched 2D MoS_2 Thin Films Grown by Chemical Vapor Deposition for Enhanced Catalytic Performance," *ACS Catal.,* vol. 7, no. 1, pp. 877-886, 2017.

[28] Y. Li, H. Wang, L. Xie, Y. Liang, G. Hong, and H. Dai, "MoS_2 Nanoparticles Grown on Graphene: An Advanced Catalyst for the Hydrogen Evolution Reaction," *J. Am. Chem. Soc,* vol. 133, no. 19, pp. 7296-7299, 2011, doi: 10.1021/ja201269b.

[29] Y. Shi *et al.*, "Energy Level Engineering of MoS_2 by Transition-Metal Doping for Accelerating Hydrogen Evolution Reaction," *J. Am. Chem. Soc.,* vol. 139, no. 43, pp. 15479-15485, 2017, doi: 10.1021/jacs.7b08881.

[30] S. Jayabal, J. Wu, J. Chen, D. Geng, and X. Meng, "Metallic 1T-MoS_2 nanosheets and their composite materials: Preparation, properties and emerging applications," *Materials Today Energy,* vol. 10, pp. 264-279, 2018.

[31] J. Xie *et al.*, "Controllable Disorder Engineering in Oxygen-Incorporated MoS_2 Ultrathin Nanosheets for Efficient Hydrogen Evolution," *J. Am. Chem. Soc.,* vol. 135, no. 47, pp. 17881-17888, 2013, doi: 10.1021/ja408329q.

[32] S. García-Dalí, J. I. Paredes, S. Villar-Rodil, A. Martínez-Jódar, A. Martínez-Alonso, and J. M. D. Tascón, "Molecular Functionalization of 2H-Phase MoS_2 Nanosheets via an Electrolytic Route for Enhanced Catalytic Performance," *ACS Appl. Mater. Interfaces,* vol. 13, no. 28, pp. 33157-33171, 2021.

[33] J. Xu, J. Zhang, W. Zhang, and C.-S. Lee, "Interlayer Nanoarchitectonics of Two-Dimensional Transition-Metal Dichalcogenides Nanosheets for Energy Storage and Conversion Applications," *Adv. Energy Mater.*, vol. 7, no. 23, p. 1700571, 2017.

[34] K. D. Rasamani, F. Alimohammadi, and Y. Sun, "Interlayer-expanded MoS_2," *Materials Today*, vol. 20, no. 2, pp. 83-91, 2017.

[35] M.-R. Gao, M. K. Y. Chan, and Y. Sun, "Edge-terminated molybdenum disulfide with a 9.4-Å interlayer spacing for electrochemical hydrogen production," *Nat. Commun*, vol. 6, no. 1, p. 7493, 2015, doi: 10.1038/ncomms8493.

[36] J. Zhou, G. Fang, A. Pan, and S. Liang, "Oxygen-Incorporated MoS_2 Nanosheets with Expanded Interlayers for Hydrogen Evolution Reaction and Pseudocapacitor Applications," *ACS Appl. Mater. Interfaces*, vol. 8, no. 49, pp. 33681-33689, 2016.

[37] A. Stergiou and N. Tagmatarchis, "Molecular Functionalization of Two-Dimensional MoS_2 Nanosheets," *Chem.Eur.J.*, vol. 24, no. 69, pp. 18246-18257, 2018.

[38] L. J. Konwar, P. Mäki-Arvela, and J.-P. Mikkola, "SO_3H-Containing Functional Carbon Materials: Synthesis, Structure, and Acid Catalysis," *Chemical Reviews*, vol. 119, no. 22, pp. 11576-11630, 2019, doi: 10.1021/acs.chemrev.9b00199.

[39] P. A. Russo *et al.*, "Solid acids with SO_3H groups and tunable surface properties: versatile catalysts for biomass conversion," *Journal of Materials Chemistry A*, vol. 2, no. 30, pp. 11813-11824, 2014, doi: 10.1039/C4TA02320J.

[40] H. G. Kang *et al.*, "Feasibility tests of $–SO_3H/–SO_3−$-functionalized magnesium phyllosilicate [$–SO_3H/–SO_3−$ MP] for environmental and bioenergy applications," *RSC Adv.*, vol. 5, no. 78, pp. 63271-63277, 2015.

[41] M. Bitaraf and A. J. R. o. C. I. Amoozadeh, "A novel sery of SO_3H-functionalized heterostructure nano-semiconductors; an efficient strategy to prepare visible-light responsive photocatalysts," *Res. Chem. Intermed.*, vol. 47, pp. 3329 - 3347, 2021.

[42] M. Zhao *et al.*, "Solvothermal synthesis of oxygen-incorporated MoS_{2-x} nanosheets with abundant undercoordinated Mo for efficient hydrogen evolution," *International Journal of Hydrogen Energy*, vol. 45, no. 38, pp. 19133-19143, 2020.

[43] D. K. Patel *et al.*, "Functionalized Graphene Tagged Polyurethanes for Corrosion Inhibitor and Sustained Drug Delivery," *ACS Biomater. Sci. Eng.*, vol. 3, no. 12, pp. 3351-3363, 2017.

[44] S. Daripa, V. K. Singh, O. Prakash, P. Maiti, B. K. Kuila, and S. Das, "Sulfonated graphene-modified electrodes for enhanced capacitive performance and improved electro-oxidation of hydrogen peroxide," *Nano-Structures & Nano-Objects*, vol. 24, p. 100531, 2020.

[45] S. Imaizumi, H. Matsumoto, M. Ashizawa, M. Minagawa, and A. Tanioka, "Nanosize effects of sulfonated carbon nanofiber fabrics for high capacity ion-exchanger," *RSC Adv.*, 10.1039/C2RA20103H vol. 2, no. 7, pp. 3109-3114, 2012.

[46] S. Kumar, A. Kumar, V. Navakoteswara Rao, A. Kumar, M. V. Shankar, and V. Krishnan, "Defect-Rich MoS_2 Ultrathin Nanosheets-Coated Nitrogen-Doped ZnO Nanorod Heterostructures: An Insight into in-Situ-Generated ZnS for Enhanced Photocatalytic Hydrogen Evolution," *ACS Appl. Energy Mater.*, vol. 2, no. 8, pp. 5622-5634, 2019.

[47] A. Gopalakrishnan, L. Durai, J. Ma, C. Y. Kong, and S. Badhulika, "Vertically Aligned Few-Layer Crumpled MoS_2 Hybrid Nanostructure on Porous Ni Foam toward Promising Binder-Free Methanol Electro-Oxidation Application," *Energy & Fuels*, vol. 35, no. 12, pp. 10169-10180, 2021.

[48] D. L. Eldridge, B. O. Mysen, and G. D. Cody, "Experimental estimation of the bisulfite isomer quotient as a function of temperature: Implications for sulfur isotope

fractionations in aqueous sulfite solutions," *Geochim. Cosmochim. Acta*, vol. 220, pp. 309-328, 2018.

[49] B. Sun *et al.*, "The fabrication of 1D/2D CdS nanorod@Ti_3C_2 MXene composites for good photocatalytic activity of hydrogen generation and ammonia synthesis," *Chemical Engineering Journal*, vol. 406, p. 127177, 2021.

[50] D. Zhang *et al.*, "High performance catalytic distillation using CNTs-based holistic catalyst for production of high quality biodiesel," *Sci. Rep.*, vol. 4, 1, 4021, 2014.

[51] H. Yu, Y. Jin, Z. Li, F. Peng, and H. Wang, "Synthesis and characterization of sulfonated single-walled carbon nanotubes and their performance as solid acid catalyst," *Journal of Solid State Chemistry*, vol. 181, no. 3, pp. 432-438, 2008.

[52] A. Banerjee, S. Chattopadhyay, A. Kundu, R. K. Sharma, P. Maiti, and S. Das, "Vertically aligned zinc oxide nanosheet for high-performance photocatalysis of water pollutants," *Ceramics International*, vol. 45, no. 14, pp. 16821-16828, 2019.

[53] G. S. Das, J. P. Shim, A. Bhatnagar, K. M. Tripathi, and T. Kim, "Biomass-derived Carbon Quantum Dots for Visible-Light-Induced Photocatalysis and Label-Free Detection of Fe(III) and Ascorbic acid," *Sci. Rep.*, vol. 9, no. 1, p. 15084, 2019.

[54] M. I. Litter, "Heterogeneous photocatalysis: Transition metal ions in photocatalytic systems," *Applied Catalysis B: Environmental*, vol. 23, no. 2, pp. 89-114, 1999.

[55] A. Ajmal, I. Majeed, R. N. Malik, H. Idriss, and M. A. Nadeem, "Principles and mechanisms of photocatalytic dye degradation on TiO_2 based photocatalysts: a comparative overview," *RSC Adv.*,vol. 4, no. 70, pp. 37003-37026, 2014.